Magnetism-induced topological transition in EuAs3

Erjian Cheng
Fudan University
Wei Xia
ShanghaiTech University
Jie Xu
Harbin Institute of Technology
Chengwei Wang
ShanghaiTech University
Chuanying Xi
High Magnetic Field Laboratory, Chinese Academy of Sciences and Collaborative Innovation Center of Advanced Microstructures
Shaowen Xu
Shanghai University
Darren Peets
TU Dresden https://orcid.org/0000-0002-5456-574X
Linshu Wang
Fudan University
Hao Su
ShanghaiTech University
Li Pi
Hefei Institute for Physical Science
Wei Ren
International Center for Quantum and Molecular Structures, Materials Genome Institute, Physics Department, Shanghai University, Shanghai 200444 https://orcid.org/0000-0001-7317-3867
Xia Wang
ShanghaiTech University
Na Yu
ShanghaiTech University
Yulin Chen
ShanghaiTech University
Weiwei Zhao
Harbin Institute of Technology Shenzhen https://orcid.org/0000-0002-0373-1146
Zhongkai Liu
ShanghaiTech University

Yanfeng Guo
ShanghaiTech University, Shanghai 201210, China https://orcid.org/0000-0002-9386-4857
Shiyan Li (✉ **shiyan_li@fudan.edu.cn**)
Fudan University https://orcid.org/0000-0001-9160-1968

Article

Keywords:

Posted Date: November 9th, 2020

DOI: https://doi.org/10.21203/rs.3.rs-100461/v1

Version of Record: A version of this preprint was published at Nature Communications on November 30th, 2021. See the published version at https://doi.org/10.1038/s41467-021-26482-7.

Magnetism-induced topological transition in EuAs$_3$

Erjian Cheng[1,*], Wei Xia[2,3,*], Xianbiao Shi[4,5,*], Chengwei Wang[2,6,*], Chuanying Xi[7], Shaowen Xu[8], Darren C. Peets[9,10], Linshu Wang[1], Hao Su[2], Li Pi[7], Wei Ren[8], Xia Wang[2], Na Yu[2], Yulin Chen[2,3,11], Weiwei Zhao[4,5], Zhongkai Liu[2,3,#], Yanfeng Guo[2,¶], and Shiyan Li[1,12,§]

[1]*State Key Laboratory of Surface Physics, Department of Physics, and Laboratory of Advanced Materials, Fudan University, Shanghai 200433, China*

[2]*School of Physical Science and Technology, ShanghaiTech University, Shanghai 200031, China*

[3]*ShanghaiTech Laboratory for Topological Physics, Shanghai 201210, China*

[4]*State Key Laboratory of Advanced Welding & Joining and Flexible Printed Electronics Technology Center, Harbin Institute of Technology, Shenzhen 518055, China*

[5]*Key Laboratory of Micro-systems and Micro-structures Manufacturing of Ministry of Education, Harbin Institute of Technology, Harbin 150001, China*

[6]*State Key Laboratory of Functional Material for Informatics, Shanghai Institute of Microsystem and Information Technology, Chinese Academy of Sciences, Shanghai 200050, China*

[7]*Anhui Province Key Laboratory of Condensed Matter Physics at Extreme Conditions, High Magnetic Field Laboratory of the Chinese Academy of Sciences, Hefei, Anhui 230031, China*

[8]*Department of Physics, Shanghai University, Shanghai 200444, China*

[9]*Ningbo Institute of Materials Technology and Engineering, Chinese Academy of Sciences, Ningbo, Zhejiang 315201, China*

[10]*Institute for Solid State and Materials Physics, Technical University of Dresden, 01062 Dresden, Germany*

[11]*Department of Physics, University of Oxford, Oxford, OX1 3PU, United Kingdom*

[12]*Collaborative Innovation Center of Advanced Microstructures, Nanjing 210093, China*

The nature of the interaction between magnetism and topology in magnetic topological semimetals remains mysterious, but may be expected to lead to a variety of novel physics. We present *ab initio* band calculations, electrical transport and angle-resolved photoemission spectroscopy (ARPES) measurements on the magnetic semimetal $EuAs_3$, demonstrating a magnetism-induced topological transition from a topological nodal-line semimetal in the paramagnetic or the spin-polarized state to a topological massive Dirac metal in the antiferromagnetic (AFM) ground state at low temperature, featuring a pair of massive Dirac points, inverted bands and topological surface states on the (010) surface. Shubnikov-de Haas (SdH) oscillations in the AFM state identify nonzero Berry phase and a negative longitudinal magnetoresistance (*n*-LMR) induced by the chiral anomaly, confirming the topological nature predicted by band calculations. When magnetic moments are fully polarized by an external magnetic field, an unsaturated and extremely large magnetoresistance (XMR) of ~ 2×10^5 % at 1.8 K and 28.3 T is observed, likely arising from topological protection. Consistent with band calculations for the spin-polarized state, four new bands in quantum oscillations different from those in the AFM state are discerned, of which two are topologically protected. Nodal-line structures at the *Y* point in the Brillouin zone (BZ) are proposed in both the spin-polarized and paramagnetic states, and the latter is proven by ARPES. Moreover, a temperature-induced Lifshitz transition accompanied by the emergence of a new band below 3 K is revealed. These results indicate that magnetic $EuAs_3$ provides a rich platform to explore exotic physics arising from the interaction of magnetism with topology.

Topological semimetals (TSMs) including Dirac, Weyl, nodal-line, and triple-point semimetals, can be divided into two categories—non-magnetic and magnetic TSMs depending on whether magnetism is involved[1-3]. Compared with better-known non-magnetic TSMs, magnetic TSMs have unique properties due to their broken time-reversal symmetry (TRS): for example, nonzero net Berry curvatures which can induce anomalous Hall or Nernst effects, only one pair of Weyl nodes for some magnetic Weyl semimetals, and a good ability to manipulate the spin for spintronics applications[3]. Moreover, when magnetism is involved, interactions of the external magnetic field with the magnetic moments can result in exotic properties, such as Weyl states induced by magnetic exchange[4,5]. However, in contrast to non-magnetic TSMs, theoretical predictions and experimental studies on magnetic TSMs are rarer and more difficult due to the complexity of the magnetic configuration for calculations and the difficulty in synthesis of single crystals[3]. In fact, the very nature of the interaction between magnetism and topology in magnetic TSMs remains mysterious. Given how few such compounds are known, seeking and fully characterizing new magnetic TSMs is a priority for the new light they may shed on these issues.

Recently, the non-magnetic CaP_3 family of materials was proposed as potential host of topological nodal-line (TNL) semimetals[6], among which $SrAs_3$ possesses a TNL feature at ambient pressure[7-9] and exotic properties under high pressure[10]. Isostructural with $SrAs_3$, $EuAs_3$ orders in an incommensurate AFM state at T_N = 11 K, and then undergoes an incommensurate-commensurate lock-in phase transition at T_L = 10.3 K, producing a collinear AFM ground state[11-16]. Previous electrical transport studies found an extremely anisotropic MR, which is strongly related to the magnetic configuration of $EuAs_3$ [17]. However, experiments sensitive to the topology have not been reported on $EuAs_3$.

In this paper, we demonstrate a magnetism-induced topological transition from a TNL semimetal in the paramagnetic or the spin-polarized state to a topological massive Dirac metal in the AFM ground state. First, we explore the band structure in the AFM ground state through band calculations and transport measurements, demonstrating that $EuAs_3$ is a magnetic topological massive Dirac metal. Second, SdH oscillations and band calculations in the spin-polarized state are displayed, yielding a proposal that $EuAs_3$ is a TNL semimetal with an XMR of ~ 2×10^5 % at 1.8 K and 28.3 T. Third, our ARPES results in the paramagnetic state verify the nodal-line structure as predicted by band calculations. Ultimately, the origin of the XMR and a temperature-induced Lifshitz transition are revealed.

Results

Topological properties in the AFM state. $EuAs_3$ crystallizes in a monoclinic structure (space group *C*2/*m*, No. 12), and the magnetic moments of Eu^{2+} are oriented parallel and antiparallel to the monoclinic *b* axis [11-16], as plotted in Fig. 1(a). Methods for single-crystal growth, experiments, and band calculations can be found in the Supplemental Information[18]. Figure 4(c) shows the bulk BZ of $EuAs_3$ and Fig. 1(b) shows the bulk and (110) surface BZs in the doubled unit cell corresponding to its antiferromagnetic ground state. The calculated band structure including spin-orbit coupling (SOC) in this magnetic ground state as determined by neutron diffraction experiments[12] for $EuAs_3$ is displayed in Fig. 1(c). In addition to topological bands around the Γ point, several trivial bands cross the Fermi level, indicating that $EuAs_3$ is a metal rather than a semimetal. In magnetic systems, TRS is broken. To preserve the Dirac node, extra symmetries, for example the combination of inversion (I) and time-reversal (T) symmetries, i.e., IT, are necessary[3]. The Dirac band crossing is not topologically protected, and it can be gapped out by SOC to turn into a gapped dispersion of massive Dirac fermions[3]. Following this clue, two massive Dirac points around Γ point are identified, as shown in the inset to Fig. 1(c). The complicated Fermi surface is composed of two hole sheets and one electron sheet in the AFM state (Fig. 1(d)), all of three-dimensional (3D) character. The electron sheet consists of two individual pockets, i.e., electron_1 and electron_2, which can both be detected by quantum oscillations.

Projected band structure analysis shows that the low energy states near the Fermi level are dominated by As-4*p* states (Fig. 1(e)). There are clear signatures of band inversion between As-$p_{x,y}$ and As-p_z orbitals at the Γ point. To identify the topological character, we calculated the Z_2 invariant by employing the Willson loop method[19]. Figures 1(f) and 1(g) show the evolution of the Wannier charge center (WCC) on two representative planes of the bulk BZ. From the calculations, the Z_2 invariant for the $k_z = 0$ plane is 1, whereas Z_2 is 0 for the $k_z = 0.5$ plane, providing strong evidence for nontrivial topology. Moreover, topologically-protected surface states are expected, and we can unambiguously identify nontrivial surface states in the surface spectrum for the semi-infinite (010) surface, as displayed in Fig. 1(h), confirming further the nontrivial topology in the AFM state.

	F (T)	E_F (meV)	A_F (10^{-3} Å^{-2})	k_F (10^{-2} Å^{-1})	v_F (10^5 m/s)	m^* (m_0)	T_D (K)
α	156	0.6	14.9	6.9	1.3	0.580(1)	15.2(4)
β	185	0.8	17.7	7.5	1.8	0.45(1)	5.0(6)
γ^1	217	1.0	20.8	8.1	2.3	0.38(3)	8(1)
γ^2	7	2.1	0.3	1.0	0.6	0.178(6)	8.0(5)
ξ	93	4.0	8.9	5.3	1.7	0.37(1)	12(2)
α'	158	3.1	15.2	6.9	1.6	0.51(1)	5.9(1)
ε	346	4.5	33.3	10.3	3.6	0.329(4)	13.1(6)
η	597	4.0	57.4	13.5	4.2	0.370(3)	9.8(7)

Table I. Parameters derived from quantum oscillations for EuAs$_3$.

To verify the predictions from band calculations, we conducted electrical transport measurements. Resistivity in zero magnetic field is plotted in Fig. 2(a), which displays typical metallic behaviour with a low-temperature peak corresponding to the magnetic transitions. The magnetic transitions were also found by thermodynamic measurements (Fig. S1) to be consistent with previous reports[11-16,18]. The inset to Fig. 2(a) shows the fit to the resistivity data below 2.5 K using a power law: $\rho = \rho_0 + AT^2$, where ρ_0 is the residual resistivity, and A the electronic scattering coefficient. The fit gives a residual resistivity ρ_0 of 2.6 $\mu\Omega$cm, and the residual resistivity ratio (RRR) ρ_{300K}/ρ_0 is ~72. Figure 2(b) shows the low-field MR data with evident SdH oscillations. B_M in Fig. 2(b) denotes the critical field, above which the spins are fully polarized by the external magnetic field. The SdH oscillation amplitude can be described by the Lifshitz-Kosevich (LK) formula[1,2]: $\Delta\rho_{xx} \propto \frac{2\pi^2 k_B T/\hbar\omega_c}{\sinh(2\pi^2 k_B T/\hbar\omega_c)} e^{2\pi^2 k_B T_D/\hbar\omega_c} \cos 2\pi\left(\frac{F}{B} - \gamma + \delta\right)$, where $\omega_c = eB/m^*$ is the cyclotron frequency and T_D is the Dingle temperature. $\gamma = \frac{1}{2} - \left(\frac{1}{2\pi}\right)\phi_B$ ($0 \leq \gamma \leq 1$) is the Onsager phase factor, and ϕ_B is a geometrical phase known as the Berry phase. For a topological system with peculiar electron state degeneracy and intra-band coupling, a π Berry phase will be observed. $2\pi\delta$ is an additional phase shift resulting from the curvature of the Fermi surface in the third direction, where δ varies from 0 to ±1/8 for a quasi-2D cylindrical Fermi surface and a corrugated 3D Fermi surface, respectively[7,8]. The cyclotron effective mass m^* can be obtained from the thermal damping factor $R_T = \frac{2\pi^2 k_B T/\hbar\omega_c}{\sinh(2\pi^2 k_B T/\hbar\omega_c)}$.

By analyzing the oscillatory component (inset to Fig. 2(c)) below B_M via fast Fourier transform (FFT), four bands are uncovered, i.e., 156, 185, 217 and 7 T, referred to as α, β, γ^1, and γ^2, respectively, in line with the band calculations. To check their topological nature, a Landau index fan diagram is plotted in Fig. 2(d), yielding intercepts of 0.6(2), 0.5(1), -0.03(9), and 0.07(8) for α, β, γ^1, and γ^2, respectively. Throughout this paper, we assign integer indices to the $\Delta\rho_{xx}$ peak positions in $1/B$ and half integer indices to the $\Delta\rho_{xx}$ valleys. According to the Lifshitz-Onsager quantization rule for a corrugated 3D Fermi surface, intercepts falling between -1/8 and 1/8 suggest nonzero Berry phase, while intercepts in the range 3/8~5/8 indicate trivial band topology. Therefore, the γ^1 and γ^2 bands are topologically protected, while the other two are trivial. Other parameters for these four bands, such as the Fermi energy E_F , extremal cross-sectional areas A_F, Fermi momentum k_F, Fermi velocity v_F, cyclotron effective mass m^* and Dingle temperature T_D, are calculated and summarized in Table I.

In TSMs, in addition to nonzero Berry phase, the *n*-LMR induced by the chiral anomaly can also serve as a smoking gun for nontrivial topology[20-22]. Figure 2(e) displays the *n*-LMR of $EuAs_3$ with magnetic field parallel to the electric current *I*. The kinks in the *n*-LMR curves below the ordering temperature arise from the field-induced transitions[15-17], i.e., from a collinear antiferromagnetic phase to incommensurate and commensurate spiral phases[15-17]. Negative MR in magnetic systems is not uncommon[20-22], when the applied magnetic field suppresses the inelastic magnetic scattering from local moments or magnetic impurities, leading to a negative MR for charge transport along all directions[20-22]. However, in $EuAs_3$ we only observed a *n*-LMR when the magnetic field is applied parallel to the electric current (Fig. S2)[18]. Furthermore, if the applied external magnetic field has a strong effect on the magnetic scattering and induces a n-LMR, the changes in the *n*-LMR will occur predominantly below and above the ordering temperature. This is not observed. Instead, we find several minor kinks arising from the magnetic transitions, on top of a much larger signal. Therefore, the suppression of magnetic scattering can be excluded as the origin of the *n*-LMR in $EuAs_3$. The *n*-LMR also displays a wide variety of temperature dependences, ruling out current jetting effects and the weak localization effect[20-22]. Since nontrivial band topology has been confirmed in $EuAs_3$, the chiral anomaly arising from Weyl fermions is the most likely mechanism behind the *n*-LMR.

The *n*-LMR induced by the chiral anomaly in TSMs can be analyzed through the Adler-Bell-Jackiw (ABJ) chiral anomaly equation[20-22]: $\sigma(B) = (1 + C_w B^2)(\sigma_0 + a\sqrt{B}) + \sigma_N$, where σ_0, C_w and $\sigma_N^{-1} = \rho_0 + AB^2$ denote the conductivity at zero field, a temperature-dependent positive parameter originating from chiral anomaly, and the conventional nonlinear band contribution around Fermi energy, respectively. Figure 2(f) shows the conductivity and the fit to the data below 3 T at various temperatures. The data above the ordering temperature are well described by the ABJ equation, while the data at lower temperatures don't fit as well, which may be ascribed to the effect that magnetic transitions have on the chiral current. The inset to Fig. 2(f) shows the temperature dependence of C_w. At 2 K, C_w is 0.253(7) T^{-2}. With increasing temperature, a clear anomaly in C_w around the ordering temperature can be observed, verifying the proposal above. When T > T_N, C_w decreases monotonically, as observed in $SrAs_3$ [7]. Taken together, these results demonstrate that $EuAs_3$ is a magnetic topological massive Dirac metal in its AFM ground state.

Topological nodal-line structure in the spin-polarized state. We now turn to the exploration of topology in the spin-polarized state, where in Fig. 1(b) we have already observed a clear change in the quantum oscillations. Figure 3(a) plots the MR of $EuAs_3$ in higher magnetic field, and an unsaturated XMR ～2×10^5 % at 1.8 K and 28.3 T is observed. By analyzing the oscillatory components above B_M (inset in Fig. 3(b)), frequency components are identified at F = 93, 158, 346, and 597 T, which are referred to here as the ξ, α', ε, and η bands, respectively (Fig. 3(b)). These four bands are different from those in lower field (Fig. 2(c)), indicating that they are likely rooted in different band structure. This is unsurprising since the unit cell is no longer doubled by antiferromagnetism, but the field-induced spin polarization can also play a significant role. We thus conducted band calculations for the field-polarized state (Fig. S3) and the paramagnetic state (Fig. S4), and these are indeed quite different, as we discuss in more detail in the Supplemental Information[18]. In the field-polarized state we find four Fermi surface sheets—two electron and two hole sheets and double nodal loops at the Y point, one each for the spin-up and spin-down channels (Fig. S3(d))[18]. To identify the topological nature of the four bands seen in quantum oscillations, a Landau index fan diagram is plotted in Fig. 3(c), and the intercepts are -0.0(1), 0.67(3), 0.34(4), and 0.61(4) for the ξ, α', ε, and η bands, respectively. The intercepts indicate that the ξ band is topologically protected, while the α' and η bands are topologically trivial. The intermediate value for ε is suggestive of a nontrivial Berry phase, but does not allow a strong conclusion, and will require further verification. The cyclotron effective masses m^* for these four pockets can be obtained by fitting the temperature dependence of the normalized FFT amplitude, as shown in the right inset to Fig. 3(c). Other parameters can be also extracted, and all values are summarized in Table I.

To better reveal the Fermi surface anisotropy and topology of $EuAs_3$, angle-dependent MR measurements

have been performed at 1.8 K, in the experimental geometry shown in the inset to Fig. 3(d). Upon rotating sample from 0° to 90°, the magnitude of the MR is reduced monotonically, as also seen in a polar plot of the

MR (Fig. S2(b))[18]. We extract the frequency components for the ξ, α', ε, and η bands by analyzing the oscillatory component (Fig. 3(e)) and summarize the results in Fig. 3(f). The angle dependence of the ξ, α', and η bands is of 3D character, while the ε band is well described below 50° by the formula F =

$F_{3D}+F_{2D}/\cos(\theta)$, where F_{2D} and F_{3D} denote 2D and 3D components. The ratio between the 2D and 3D components derived from the fit (F2D/F3D) is ~ 1.76, suggesting that the ε pocket exhibits mainly 2D character although a 3D component also exists.

Now, we turn to the angle dependence of the Berry phase. As shown in Fig. 3(g), the intercept for the topological ξ band shows strong angle dependence, similar to results in other systems such as Cd_3As_2 [23], ZrSi*M* (*M* = Se, Te)[24], or $ZrTe_5$ [25]. For $\vartheta < 30°$ and $\vartheta \geq 60°$, the intercept falls between -1/8 and 1/8, while it falls between 3/8 and 5/8 for $30° \leq \vartheta < 60°$. For the ε band, the intercept from 0° to 70° fluctuates between 1/8 and 5/8, averaging to 0.34(5), which is suggestive of trivial topology. However, when ϑ reaches 80° and 90°, this intercept falls between -1/8 and 1/8, implying nonzero Berry phase. For η and α' bands, the intercepts at all angles remain between 1/8 and 5/8, averaging 0.4(2) and 0.5(2), respectively, indicating trivial topology.

Topological nodal-line structure in the paramagnetic state. Since our band structure calculations identify nodal loops at *Y* and our quantum oscillation data indicate nontrivial band topology, we also directly investigated the band structure with ARPES. Momentum analysis in this technique is incompatible with magnetic field, so we investigated the paramagnetic rather than the field-polarized state; however, as shown in more detail in supplementary Figs. S3 and S4, a closed nodal loop persists at the *Y* point in the paramagnetic state[18]. In order to visualize the nodal loop in $EuAs_3$, the photon energy dependence of the electronic structure along the k_y direction was investigated at 18 K within the vertical plane of the (010) cleaved surface, as sketched in Fig. 4(c). From the intensity plot of the Fermi surface in the k_y-k_z plane (Fig. 4(a)), the pocket centered at the *Y* point (17 eV) can be easily identified, and two nodes arising from the crossing of the electronlike and holelike bands can be also observed in Fig. 4(b), which agrees with the band calculations (red lines). We estimate the Fermi momenta k_F and Fermi velocities v_F to be k_F = 0.12 and 0.14 $Å^{-1}$ and $v_F = 3.7\times10^5$ and 1.17×10^5 m/s, respectively, for the hole and electron bands, the same order of magnitude as for the ε and η bands (see Table I). For ARPES cuts away from the *Y* point (Fig. 4(b)), the band-crossing area shrinks gradually and finally disappears. This is highlighted by an orange ellipse, and represents the nodal loop predicted by our band structure calculations. These data are extremely similar to what was found in $SrAs_3$ [9].

The verification of the nodal-line structure in the paramagnetic state serves as strong evidence for the existence of nodal-line structure in the spin-polarized state, which has closely similar but spin-split band structure, but the similarities may not end there. Very recently, lifted degeneracy of the Bloch bands was observed in the paramagnetic phase of $EuCd_2As_2$, producing a spin-fluctuation-induced Weyl semimetal state[26]. The magnetic susceptibility in $EuAs_3$ reveals a positive Curie-Weiss temperature T_{CW} of 4.4 K for magnetic fields applied within the *ab* plane (Supplementary Fig. S6), suggestive of ferromagnetic fluctuations deep in the paramagnetic phase[18]. The ferromagnetic correlations in $EuAs_3$ may induce band splitting within the paramagnetic phase, which may be resolvable with higher-resolution ARPES, such as laser ARPES.

Discussion

It is clear from our transport measurements that the electronic structure in the antiferromagnetically ordered state is very different from that found in the field-polarized or paramagnetic states. This is a consequence of the doubling of the unit cell due to antiferromagnetic order and the coupling of this magnetic order to the electronic structure, and is well described by our band calculations. However, we also find evidence for an additional Lifshitz transition within the antiferromagnetic phase.

Figure 3(h) shows the Hall resistivity (ρ_{xy}) from 0.3 to 30 K. The ρ_{xy} curves are clearly nonlinear, implying the coexistence of two types of carriers, as predicted by band structure calculations. On cooling, the slope of the curve changes from positive to negative, indicating an increased contribution from electron carriers. The carrier concentration and mobility are extracted by fitting the Hall conductivity with a two-carrier model, and results are summarized in Fig. 3(i). For $3 \leq T \leq 30$ K, the concentration of hole carriers is larger than that of electron carriers. Upon decreasing the temperature below 3 K, the concentration of electron carriers is suddenly enhanced, accompanied by a sharp increase in the mobility of hole carriers. These indicate a possible Lifshitz transition. To check this, we analyze the oscillatory component ($\Delta\rho_{xy}$), and identify a new oscillation frequency of 374 T (denoted as the φ band) with trivial topology (see Fig. S5(b)), demonstrating that a Lifshitz transition does indeed occur[18]. Temperature-induced Lifshitz transitions are also observed in other TSMs, for example, $M\mathrm{Te}_5$ (M = Zr, Hf)[27,28], which have been used to explain the origin of the resistivity anomaly. However, no such anomaly can be observed in EuAs_3, indicative of its unusual origin. Generally speaking, Lifshitz transitions are related to electronic transitions at zero temperature, and involve abrupt changes of the Fermi surface topology. However, in topological materials, Lifshitz transitions can also involve other types of zero-energy modes, such as Weyl or Dirac nodes, nodal lines, flat bands, Majorana modes, etc.[29]. It has been proposed that multiple types of novel Lifshitz transitions involving Weyl points are possible depending on how they connect Fermi surfaces and pockets. For instance, the Lifshitz transition can correspond to the transfer of Berry flux between Fermi pockets connected by type-II Weyl points[30]. To understand the physics behind the apparent low-temperature Lifshitz transition in EuAs_3, more work is needed.

According to the conventional charge-carrier compensation picture for XMR, the ratio n_h/n_e should be unity[1,2]. At 0.3 K, n_h/n_e for EuAs_3 is ～1.0, consistent with this picture. However, for $3 \le T \le 30$ K, n_h/n_e varies between 1.5 and 2.5 while the MR remains large and unsaturated, evidently excluding the charge-compensation picture for EuAs_3. XMR is also frequently encountered in the cases of topologically-protected electronic band structure, and when open orbits contribute[1,2,31,32]. According to the open-orbit effect, the unsaturated XMR is only observed for current along the open orbits[32]. However, the observation of the unsaturated XMR with different current direction in EuAs_3 excludes the open-orbit effect (see Fig. S7)[18]. Beside, for both the charge-carrier compensation picture and open-orbit effect, a B^2 dependence of MR is suggested[31,32], which is different from the situation of EuAs_3 reported here (Fig. S7(c))[18]. Since we have verified nontrivial band topology in EuAs_3, we consider this the more likely explanation.

In summary, combining band calculations, electrical transport and ARPES measurements on the magnetic

compound $EuAs_3$, we report a magnetism-induced topological transition from a TNL semimetal in the paramagnetic or the spin-polarized state to a topological massive Dirac metal in the AFM ground state. The paramagnetic and spin-polarized states differ by the splitting of a topological nodal line associated with the spin-splitting of the band structure. An XMR of ～2×10^5 % and an asyet-unexplained temperature-induced Lifshitz transition below 3 K have also been revealed. These results indicate that magnetic $EuAs_3$ could serve as a unique platform to explore exotic physics at the interface of magnetism and topology.

Acknowledgements

This work is supported by the Ministry of Science and Technology of China (Grant Nos. 2015CB921401 and 2016YFA0300503), the Natural Science Foundation of China (Grant Nos. 11421404, 11674367, 11674229 and 11874264), the NSAF (Grant No. U1630248), and the Zhejiang Provincial Natural Science Foundation (Grant No. LZ18A040002), the National Key R&D program of China (Grant No. 2017YFA0305400) and the Ningbo Science and Technology Bureau (Grant No. 2018B10060). W.W.Z. is supported by the Shenzhen Peacock Team Plan (KQTD20170809110344233) and Bureau of Industry and Information Technology of Shenzhen through the Graphene Manufacturing Innovation Center (201901161514). Y.F.G. acknowledges research funds from the State Key Laboratory of Surface Physics and Department of Physics, Fudan University (Grant No. KF2019 06). C.Y.X. was supported by the Users with Excellence Project of Hefei Science Center CAS (Grant No. 2018HSC-UE015). D.C.P. is supported by the Chinese Academy of Sciences through 2018PM0036 and from the Deutsche Forschungsgemeinschaft (DFG), through project C03 of the Collaborative Research Center SFB 1143 (project-ID 247310070). The authors are grateful for support from the Analytical Instrumentation Center (# SPST-AIC10112914), SPST, ShanghaiTech University.

Author Contributions

S.Y.L. and Y.F.G. conceived the idea and designed the experiments. E.J.C. was responsible for electronic transport experiments. W.X., X.W., N.Y. and H.S. performed sample synthesis and partial data analysis. X.B.S., S.W.X., W.R. and W.W.Z. performed the electronic band calculations. C.Y.X., L.S.W. and L.P. helped the MR measurements in Hefei. C.W.W., Y.L.C., and Z.K.L. performed ARPES measurements and analysis. Z.K.L., Y.F.G. and S.Y.L. supervised the project. E.J.C., W.X., X.B.S., and C.W.W. contributed equally to this work. E.J.C., D.C.P., Y.F.G., and S.Y.L. analyzed the data and wrote the paper. All authors discussed the results and commented on the manuscript.

Additional Information: Correspondence and requests for materials should be addressed to S.Y.L. (shiyan_li@fudan.edu.cn), Y.F.G. (guoyf@shanghaitech.edu.cn) or Z.K.L. (liuzhk@shanghaitech.edu.cn).

Competing interests: The authors declare no competing interests.

Data availability: Source data that support the plots within the paper and other findings of this study are available from the corresponding authors upon reasonable request.

References

1. Armitage, N. P., Mele, E. J. and Vishwanath, A. Weyl and Dirac semimetals in three-dimensional solids. *Rev. Mod. Phys*. **90**, 015001 (2018).

2. Burkov, A. A., Hook, M. D. and Balents, L. Topological nodal semimetals. *Phys. Rev. B* **84**, 235126 (2011).

3. Zou, J. Y., He, Z. R. and Xu, G. The study of magnetic topological semimetals by first principles calculations. *npj Comput. Mater*. **5**, 96 (2019).

4. Fang, Y. *et al.* Magnetic-field-induced nontrivial electronic state in the Kondo-lattice semimetal CeSb.

Phys. Rev. B **101**, 094424 (2020).

5. Su, H. *et al.* Magnetic exchange induced Weyl state in a semimetal $EuCd_2Sb_2$. *APL Mater*. **8**, 011109 (2020).

6. Xu, Q. *et al.* Topological nodal line semimetals in CaP_3 family of materials. *Phys. Rev. B* **95**, 045136 (2017).

7. Li, S. C. *et al.* Evidence for a Dirac nodal-line semimetal in $SrAs_3$. *Sci. Bull*. **63**, 535-541 (2018).

8. An, L. L. *et al.* Chiral anomaly and nontrivial Berry phase in the topological nodal-line semimetal $SrAs_3$. *Phys. Rev. B* **99**, 045143 (2019).

9. Song, Y. K. *et al.* Photoemission spectroscopic evidence for the Dirac nodal line in monoclinic semimetal $SrAs_3$. *Phys. Rev. Lett.* **124**, 056402 (2020).

10. Cheng, E. J. *et al.* Pressure-induced superconductivity and topological phase transitions in the topological nodal-line semimetal $SrAs_3$. *npj Quantum Mater*. **5**, 38 (2020).

11. Bauhofer, W., Wittmann, M. and Schnering, H. G. v. Structure, electrical and magnetic properties of $CaAs_3$, $SrAs_3$, $BaAs_3$ and $EuAs_3$. *J. Phys. Chem. Solids* **42**, 687-695 (1981).

12. Chattopadhyay, T., Schnering, H. G. v. and Brown, P. J. Neutron diffraction study of the magnetic ordering in $EuAs_3$. *J. Magn. Magn. Mater.* **28**, 247-249 (1982).

13. Chattopadhyay, T. and Brown, P. J. Field-induced transverse-sine-wave-to-longitudinal-sine-wave transition in $EuAs_3$. *Phys. Rev. B* **38**, 795 (1988).

14. Chattopadhyay, T., Liss, K. D. and Brückel, T. Incommensurate-commensurate lock-in phase transition in $EuAs_3$. *J. Magn. Magn. Mater.* **177**, 1058-1060 (1998).

15. Chatterji, T. *et al.* High-energy non-resonant X-ray magnetic scattering from $EuAs_3$. *Solid State Commun.* **131**, 713-717 (2004).

16. Chatterji, T. and Henggeler, W. μSR investigation of the magnetic ordering in $EuAs_3$. *Solid State Commun.* **132**, 617-622 (2004).

17. Bauhofer, W. and McEwer, K. A. Anisotropic magnetoresistance of the semimetallic antiferromagnet

$EuAs_3$. *Phys. Rev. B* **43**, 13450-13455 (1991).

18. Supplemental Information for “Magnetism-induced topological transition in $EuAs_3$”.

19. Yu, R. *et al.* An equivalent expression of Z_2 Topological invariant for band insulators using non-Abelian Berry’s connection. *Phys. Rev. B* **84**, 075119 (2011).

20. Kuroda, K. *et al.* Evidence for magnetic Weyl fermions in a correlated metal. *Nat. Mater.* **16**, 1090-1095 (2017).

21. Huang, X. C. *et al.* Observation of the chiral-anomaly-induced negative magnetoresistance in 3D Weyl Semimetal TaAs. *Phys. Rev. X* **5**, 031023 (2015).

22. Zhang, C. L. *et al.* Signatures of the Adler-Bell-Jackiw chiral anomaly in a Weyl fermion semimetal. *Nat. Commun*. **7**, 10735 (2016).

23. Xiang, Z. J. *et al.* Angular-Dependent Phase Factor of Shubnikovde Haas Oscillations in the Dirac Semimetal Cd_3As_2. *Phys. Rev. Lett.* **115**, 226401 (2015).

24. Hu, J. *et al.* Evidence of topological nodal line fermions in ZrSiSe and ZrSiTe. *Phys. Rev. Lett.* **117**, 016602 (2016).

25. Liu, Y. W. *et al.* Zeeman splitting and dynamical mass generation in Dirac semimetal $ZrTe_5$. *Nat. Commun.* **7**, 12516 (2016).

26. Ma, J.-Z. *et al.* Spin fluctuation induced Weyl semimetal state in the paramagnetic phase of $EuCd_2As_2$. *Sci. Adv.* **5**, eaaw4718 (2019).

27. Zhang, Y. *et al.* Electronic evidence of temperature-induced Lifshitz transition and topological nature in $ZrTe_5$. *Nat. Commun.* **8**, 15512 (2017).

28. Zhang, Y. *et al.* Temperature-induced Lifshitz transition in topological insulator candidate $HfTe_5$. *Sci. Bull.* **62**, 950-956 (2017).

29. Volovik, G. E. Topological Lifshitz transitions. *Low Temp. Phys.* **43**, 47-55 (2017).

30. Zhang, K. and Volovik, G. E. Lifshitz transitions via the type-II Dirac and type-II Weyl points. *Jetp Lett.*

105, 519-525 (2017).

31. Abrikosov, A. A. Quantum magnetoresistance. *Phys. Rev. B* **58**, 2788 (1998).

32. Zhang, S. N. *et al.* Magnetoresistance from Fermi surface topology. *Phys. Rev. B* **99**, 035142 (2019).

Figure 1

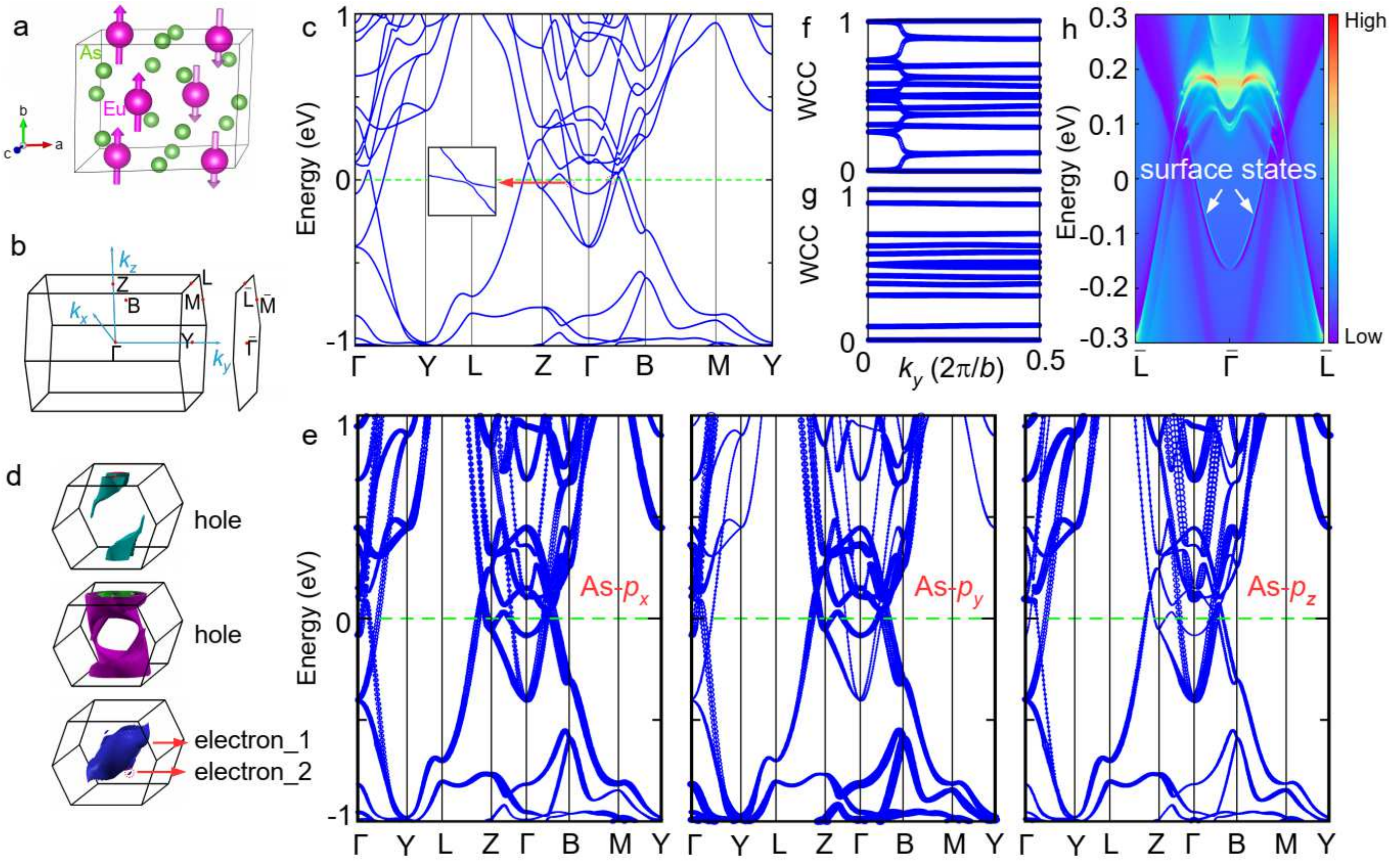
a
As
Eu
b
c
a
b
k_z
Z
L
B
M
k_x
Y
Γ
k_y
$\bar{L}$
$\bar{M}$
$\bar{\Gamma}$
c
Energy (eV)
1
0
-1
Γ Y L Z Γ B M Y
d
hole
hole
electron_1
electron_2
e
Energy (eV)
As-p_x
As-p_y
As-p_z
Γ Y L Z Γ B M Y
f
WCC
g
WCC
k_y ($2\pi/b$)
0
0.5
h
Energy (eV)
0.3
0.2
0.1
0
-0.1
-0.2
-0.3
surface states
High
Low
$\bar{L}$ $\bar{\Gamma}$ $\bar{L}$

Figure 2

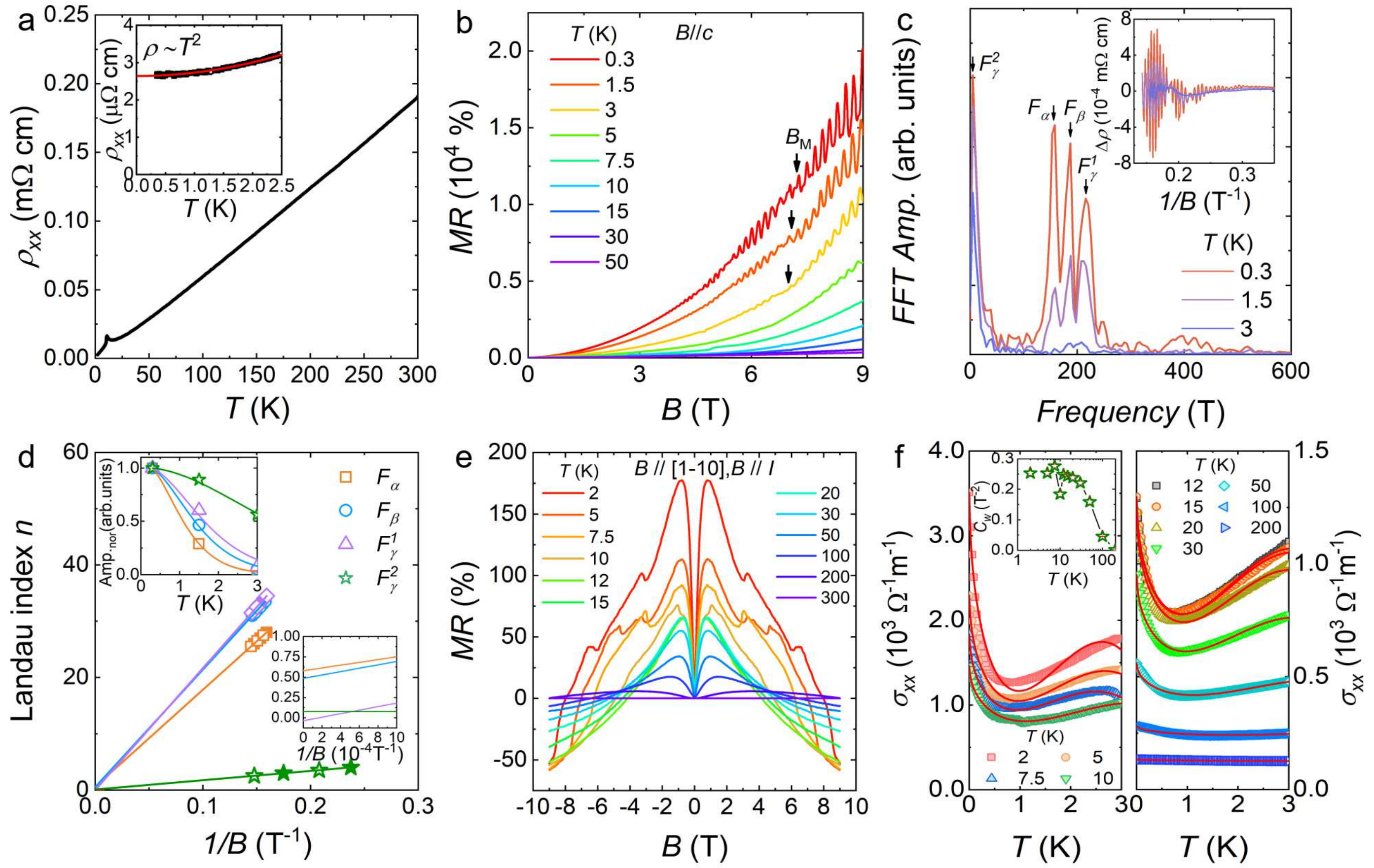
a
ρ_{xx} (mΩ cm)
T (K)
$\rho \sim T^2$
ρ_{xx} (μΩ cm)
b
T (K)
$B//c$
0.3
1.5
3
5
7.5
10
15
30
50
B_M
MR (10^4 %)
B (T)
c
F_γ^2
F_α
F_β
F_γ^1
$\Delta\rho$ (10^{-4} mΩ cm)
$1/B$ (T^{-1})
T (K)
0.3
1.5
3
FFT $Amp.$ (arb. units)
$Frequency$ (T)
d
Landau index n
$1/B$ (T^{-1})
Amp._nor (arb.units)
T (K)
F_α
F_β
F_γ^1
F_γ^2
$1/B$ ($10^{-4}T^{-1}$)
e
T (K)
B // [1-10], B // I
2
5
7.5
10
12
15
20
30
50
100
200
300
MR (%)
B (T)
f
σ_{xx} (10^3 $\Omega^{-1}m^{-1}$)
C_W (T^{-2})
T (K)
2
5
7.5
10
12
15
20
30
50
100
200
T (K)

Figure 3

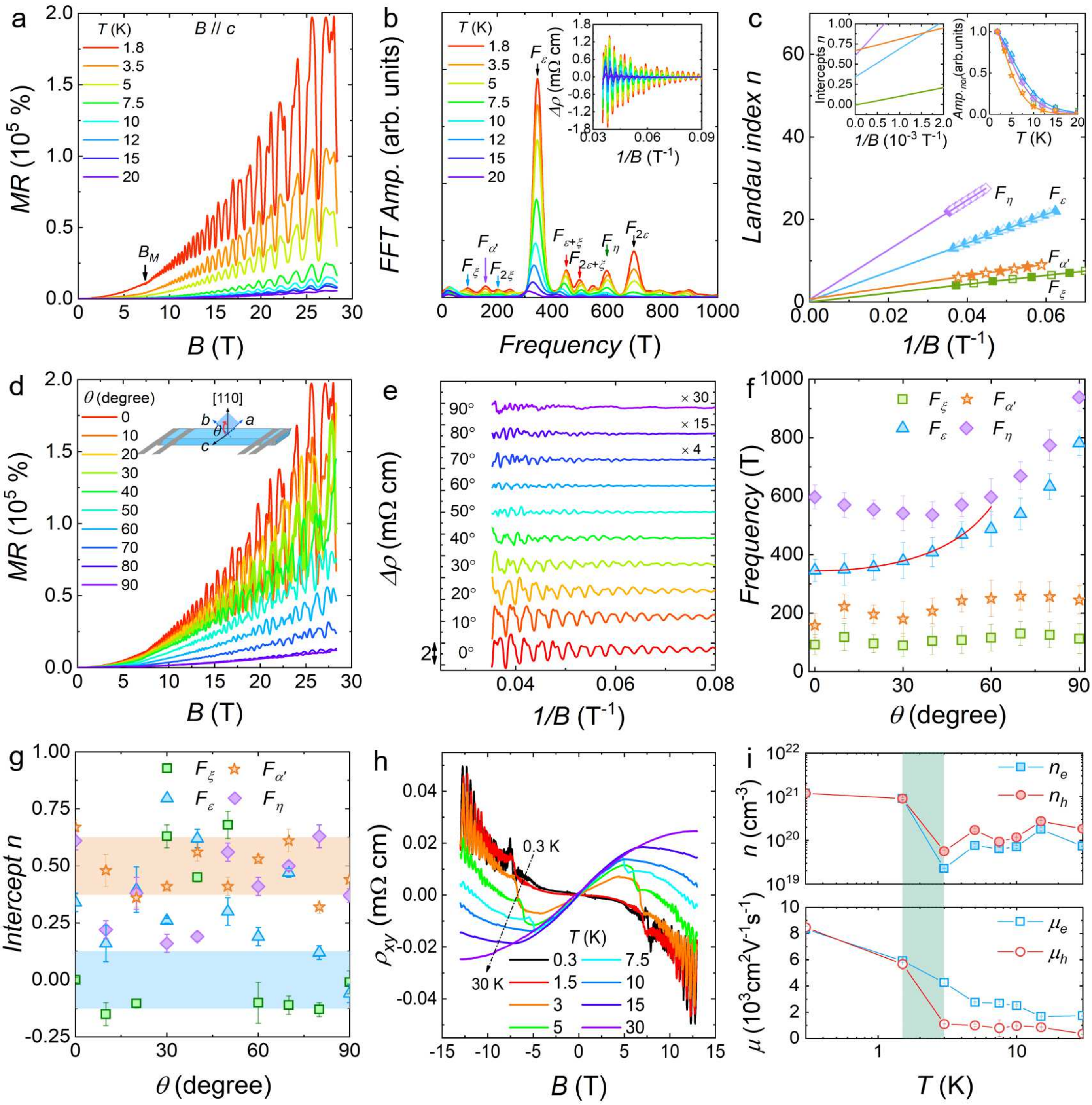
a
T (K)
B // c
1.8
3.5
5
7.5
10
12
15
20
B_M
MR (10^5 %)
B (T)
b
T (K)
1.8
3.5
5
7.5
10
12
15
20
F_ε
F_α'
F_ξ
F_2ξ
F_ε+ξ
F_2ε+ξ
F_η
F_2ε
Δρ (mΩ cm)
1/B (T^-1)
FFT Amp. (arb. units)
Frequency (T)
c
Intercepts n
1/B (10^-3 T^-1)
Amp._nor (arb.units)
T (K)
F_η
F_ε
F_α'
F_ξ
Landau index n
1/B (T^-1)
d
θ (degree)
0
10
20
30
40
50
60
70
80
90
[110]
b
a
θ
c
MR (10^5 %)
B (T)
e
90°
80°
70°
60°
50°
40°
30°
20°
10°
0°
× 30
× 15
× 4
2
Δρ (mΩ cm)
1/B (T^-1)
f
F_ξ
F_α'
F_ε
F_η
Frequency (T)
θ (degree)
g
F_ξ
F_α'
F_ε
F_η
Intercept n
θ (degree)
h
0.3 K
30 K
T (K)
0.3
1.5
3
5
7.5
10
15
30
ρ_xy (mΩ cm)
B (T)
i
n_e
n_h
n (cm^-3)
μ_e
μ_h
μ (10^3cm^2V^-1s^-1)
T (K)

Figure 4

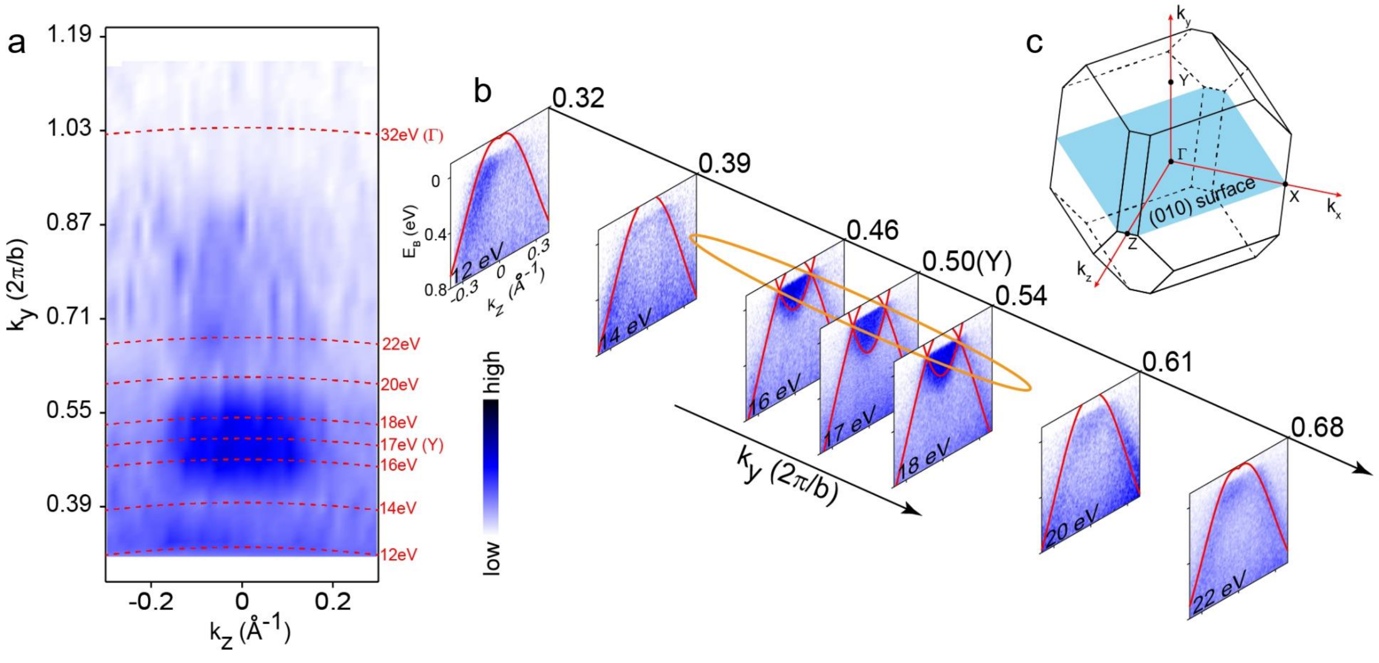

Figure captions

Figure 1 | Topological massive Dirac metal state in the antiferromagnetic state of EuAs$_3$, revealed by band

calculations. **a**, Schematic for the crystal structure of EuAs3 in the doubled magnetic unit cell. The arrows on Eu^{2+} represent the spin directions, which are parallel and antiparallel to the *b* axis. **b**, Bulk and (110)-projected surface BZs of the doubled magnetic unit cell of $EuAs_3$ with several high-symmetry points marked. **c**, Band structure of EuAs3 from GGA+SOC+*U* (*U* = 5 eV) calculations for the AFM ground state. The inset shows the massive Dirac point with a small gap. **d**, Fermi surfaces of EuAs3 derived from the band structure. **e**, Projected band structure of $EuAs_3$, where the symbol size represents the projected weight of Bloch states onto the As-p_x, p_y, and p_z orbitals as labelled. Band inversion can be observed at the Γ point. The Wannier charge center is calculated in the (**f**), $k_z = 0$ and (**g**) $k_z = 0.5$ planes. **h**, Calculated surface states on the (010) surface. The nontrivial topological surface states are clearly visible.

Figure 2 | Quantum oscillations and negative longitudinal magnetoresistance (*n*-LMR) in the antiferromagnetic state of $EuAs_3$. **a**, Resistivity of $EuAs_3$ single crystal in zero magnetic field. The inset shows the fit to the low-temperature data. **b**, MR accompanied by distinct SdH oscillations. B_M represents the critical magnetic field which induces a magnetic transition from a collinear antiferromagnetic phase to a polarized ferromagnetic phase. **c**, FFT results at various temperatures. The inset displays the oscillatory component ρ_{xx} below B_M. Four bands, i.e., α, β, γ^1 and γ^2, can be distinguished. The latter two construct one electron sheet. **d**, Landau index *n* plotted against 1/*B* for the SdH oscillations at 0.3 K. Lines represent linear fits. The right inset shows the extrapolation of 1/*B* to zero. The left inset shows the normalized FFT amplitude ($\mathrm{Amp.}_{nor}$) as a function of temperature, and the solid lines represent fits to the Lifshitz-Kosevich formula. **e**, *n*-LMR measured with magnetic field parallel to the electric current *I* at various temperatures. **f**, Longitudinal conductivity at various temperatures fit to the Adler-Bell-Jackiw chiral anomaly equation. The inset shows the emergence of a positive parameter originating from the chiral anomaly C_w.

Figure 3 | Quantum oscillations study in the spin-polarized state of $EuAs_3$, and Hall resistivity

measurements. a, Magnetoresistance measurements of $EuAs_3$ single crystal under higher magnetic field up to 28.3 T. **b**, FFT results at various temperatures, yielding the four bands ξ, α', ε, and η. The inset displays the oscillatory component ρ_{xx} above B_M. **c**, Landau index n plotted against $1/B$ for the SdH oscillations at 1.8 K. The left inset shows the extrapolation of $1/B$ to zero. The right inset shows the normalized FFT amplitude (Amp.$_{nor}$) as a function of temperature, and the solid lines represent the Lifshitz-Kosevich formula fit. **d**, SdH oscillations at different angles; the inset is a schematic illustration of the experimental geometry and the angle ϑ. For $\vartheta = 0°$, the magnetic field is parallel to the c axis. For $\vartheta = 90°$, the magnetic field is applied along the [110] direction. **e**, The oscillatory component ρ_{xx} as a function of $1/B$. Angular dependence of (**f**) the FFT frequencies, where error bars represent the full widths at half maximum of the FFT peaks, and (**g**) the Landau level index intercepts. **h,** Hall resistivity at various temperatures. **i,** Carrier concentration and mobility as a function of temperature. The shadow area represents the temperature interval where a Lifshitz transition takes place.

Figure 4 | Verification of topological nodal-line structure by ARPES measurements in the paramagnetic state of $EuAs_3$. a, Photon-energy-dependent plot of photoemission intensities at the Fermi surface along the k_z direction. The red dotted lines denote the k_y momentum locations probed by different photon energies. **b**, The dispersions along the k_z direction probed by different photon energies corresponding to different k_y. The calculated electronic structure is superimposed as red curves. The orange ellipse illustrates the topologically nontrivial nodal loop. **c**, The Brillouin zone of $EuAs_3$, with high-symmetry points and (010) surface labeled.

Figures

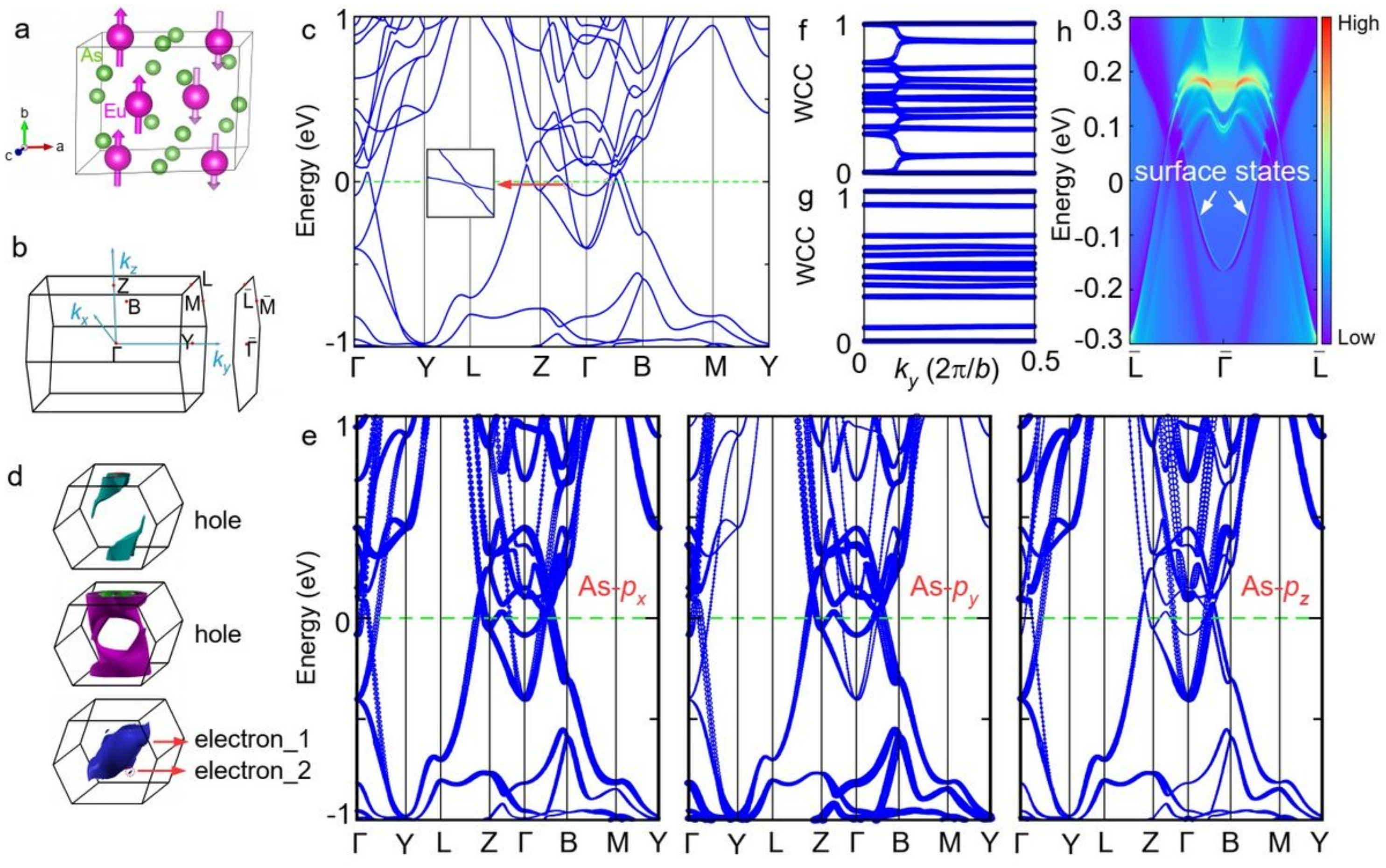

Figure 1

Topological massive Dirac metal state in the antiferromagnetic state of EuAs3, revealed by band calculations. a, Schematic for the crystal structure of EuAs3 in the doubled magnetic unit cell. The arrows on Eu2+ represent the spin directions, which are parallel and antiparallel to the b axis. b, Bulk and (110)-projected surface BZs of the doubled magnetic unit cell of EuAs3 with several high-symmetry points marked. c, Band structure of EuAs3 from GGA+SOC+U (U = 5 eV) calculations for the AFM ground state. The inset shows the massive Dirac point with a small gap. d, Fermi surfaces of EuAs3 derived from the band structure. e, Projected band structure of EuAs3, where the symbol size represents the projected weight of Bloch states onto the As-px, py, and pz orbitals as labelled. Band inversion can be observed at the Γ point. The Wannier charge center is calculated in the (f), kz = 0 and (g) kz = 0.5 planes. h, Calculated surface states on the (010) surface. The nontrivial topological surface states are clearly visible.

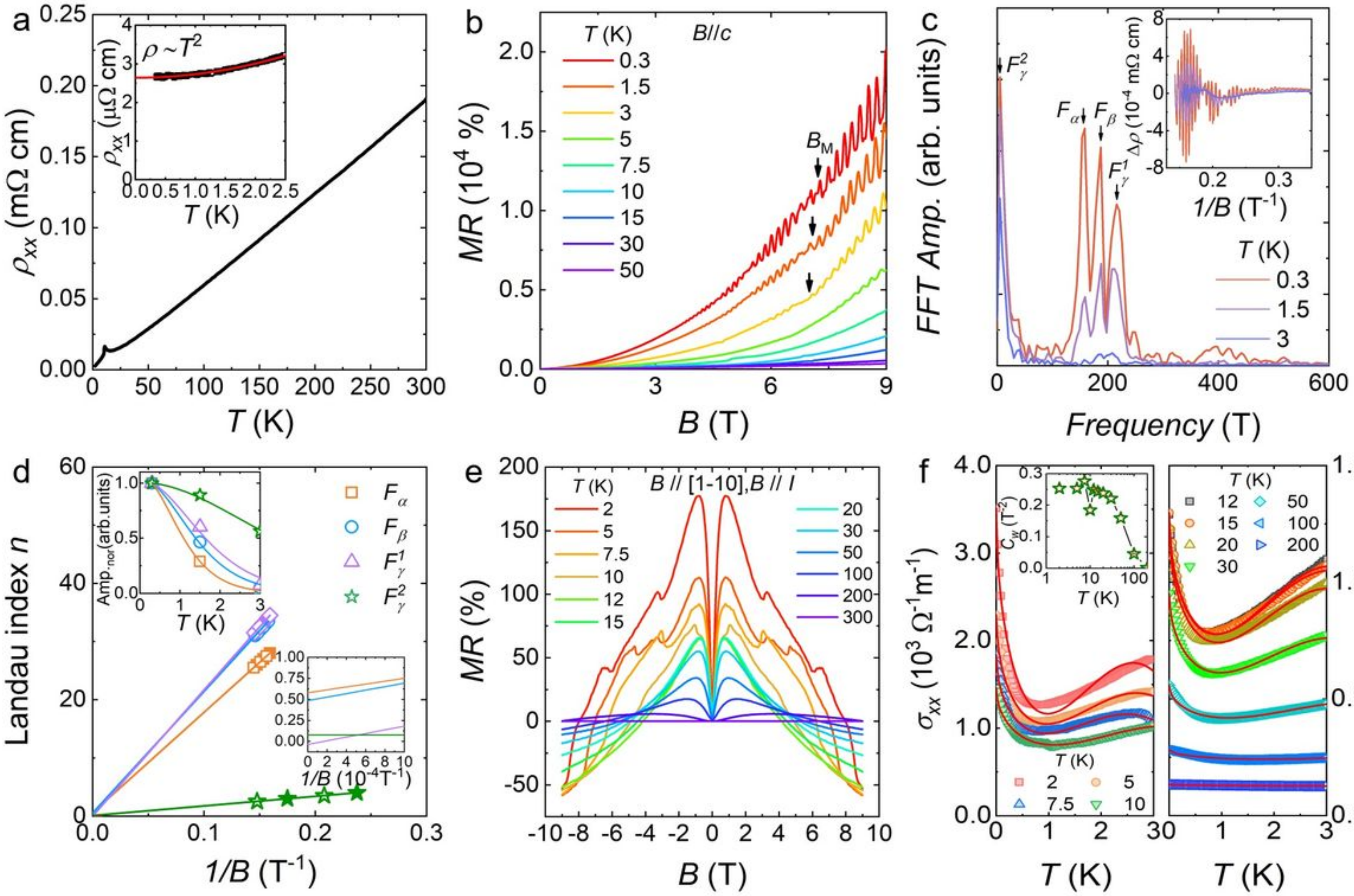

Figure 2

Quantum oscillations and negative longitudinal magnetoresistance (n-LMR) in the antiferromagnetic state of EuAs3. a, Resistivity of EuAs3 single crystal in zero magnetic field. The inset shows the fit to the low-temperature data. b, MR accompanied by distinct SdH oscillations. BM represents the critical magnetic field which induces a magnetic transition from a collinear antiferromagnetic phase to a polarized ferromagnetic phase. c, FFT results at various temperatures. The inset displays the oscillatory component ρxx below BM. Four bands, i.e., α, β, γ1 and γ2, can be distinguished. The latter two construct one electron sheet. d, Landau index n plotted against 1/B for the SdH oscillations at 0.3 K. Lines represent linear fits. The right inset shows the extrapolation of 1/B to zero. The left inset shows the normalized FFT amplitude (Amp.nor) as a function of temperature, and the solid lines represent fits to the Lifshitz-Kosevich formula. e, n-LMR measured with magnetic field parallel to the electric current I at various temperatures. f, Longitudinal conductivity at various temperatures fit to the Adler-Bell-Jackiw chiral anomaly equation. The inset shows the emergence of a positive parameter originating from the chiral anomaly Cw.

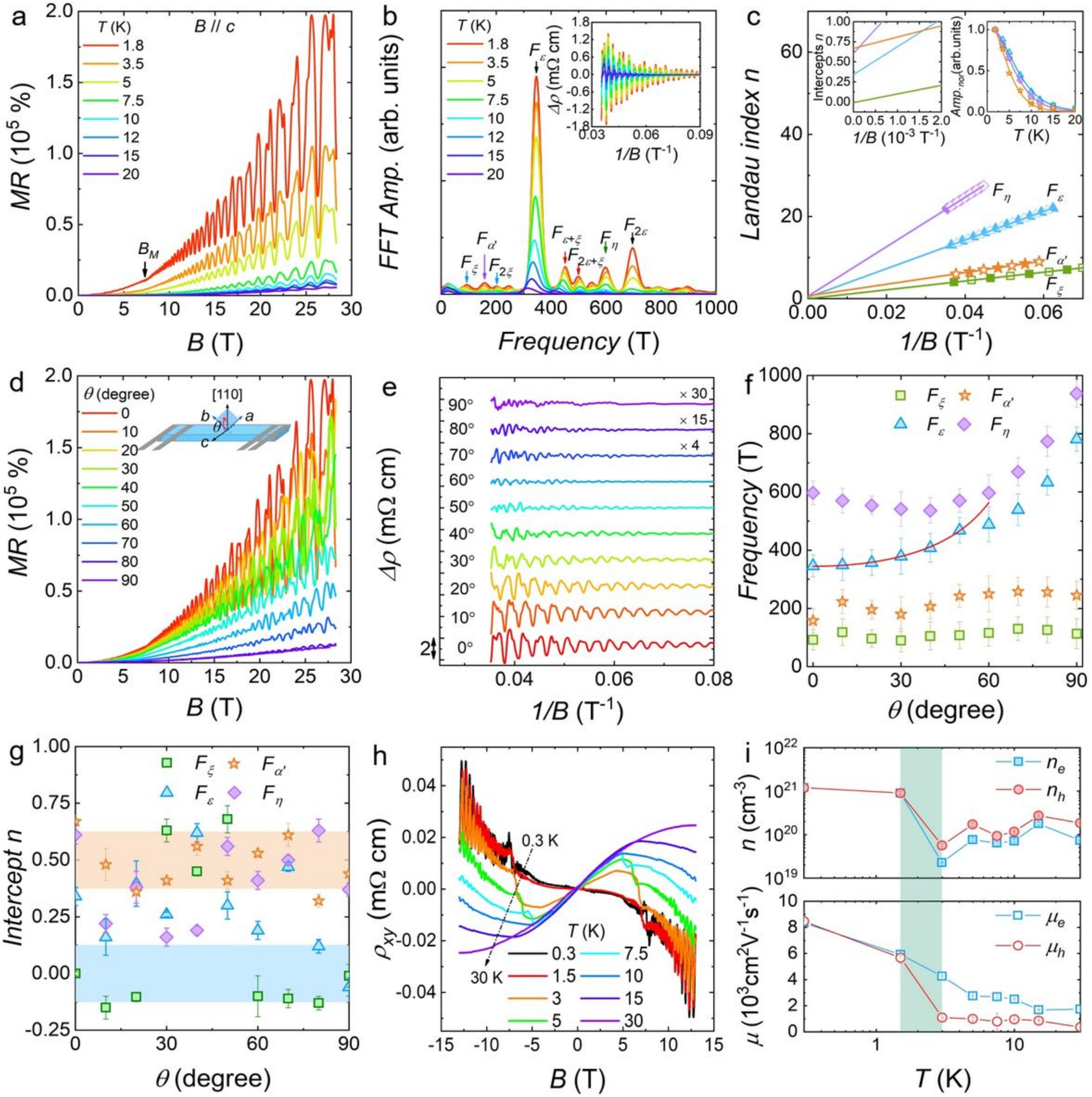

Figure 3

Quantum oscillations study in the spin-polarized state of EuAs3, and Hall resistivity measurements. a, Magnetoresistance measurements of EuAs3 single crystal under higher magnetic field up to 28.3 T. b, FFT results at various temperatures, yielding the four bands ξ, α', , and η. The inset displays the oscillatory component ρxx above BM. c, Landau index n plotted against 1/B for the SdH oscillations at 1.8 K. The left inset shows the extrapolation of 1/B to zero. The right inset shows the normalized FFT amplitude (Amp.nor) as a function of temperature, and the solid lines represent the Lifshitz-Kosevich formula fit. d, SdH oscillations at different angles; the inset is a schematic illustration of the experimental geometry and the angle θ. For θ = 0□, the magnetic field is parallel to the c axis. For θ = 90□, the magnetic field is applied along the [110] direction. e, The oscillatory component ρxx as a function of 1/B. Angular dependence of (f) the FFT frequencies, where error bars represent the full widths at half maximum of the FFT peaks, and (g) the Landau level index intercepts. h, Hall resistivity at various temperatures. i, Carrier concentration and mobility as a function of temperature. The shadow area represents the temperature interval where a Lifshitz transition takes place.

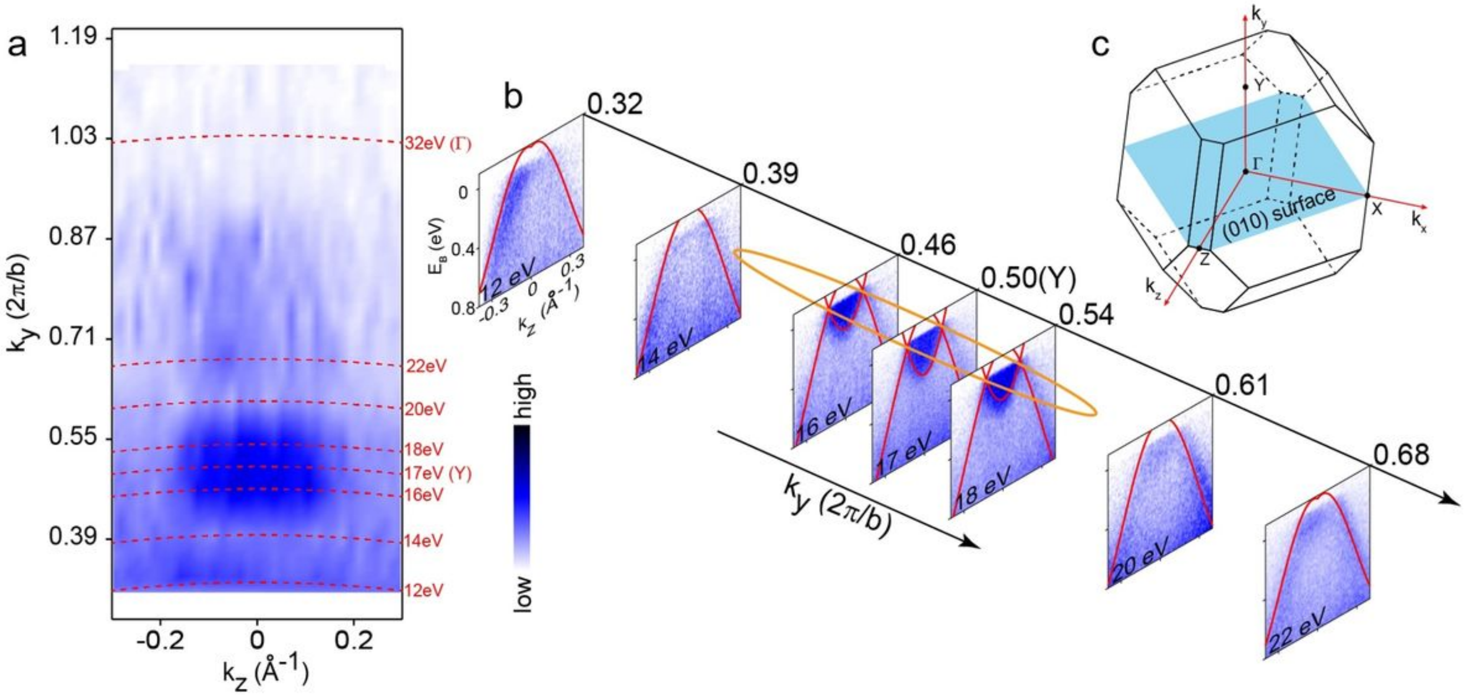

Figure 4

Verification of topological nodal-line structure by ARPES measurements in the paramagnetic state of EuAs3. a, Photon-energy-dependent plot of photoemission intensities at the Fermi surface along the kz direction. The red dotted lines denote the ky momentum locations probed by different photon energies. b, The dispersions along the kz direction probed by different photon energies corresponding to different ky. The calculated electronic structure is superimposed as red curves. The orange ellipse illustrates the topologically nontrivial nodal loop. c, The Brillouin zone of EuAs3, with high-symmetry points and (010) surface labeled.

Supplementary Files

This is a list of supplementary files associated with this preprint. Click to download.

- EuAs3SI.pdf
- FigS1.pdf
- FigS2.pdf

- FigS3.pdf
- FigS4.pdf
- FigS5.pdf
- FigS6.pdf
- FigS7.pdf